A mechanically stable and tunable cryogenic Fabry–Pérot microcavity ⊘

Y. Fontana ; R. Zifkin ; E. Janitz ; C. D. Rodríguez Rosenblueth ; L. Childress ✉

Check for updates

View Online

Export Citation

A mechanically stable and tunable cryogenic Fabry–Pérot microcavity

View Online   Export Citation   CrossMark

Y. Fontana,[1] 〔iD〕 R. Zifkin,[2] 〔iD〕 E. Janitz,[3] 〔iD〕 C. D. Rodríguez Rosenblueth,[2] 〔iD〕 and L. Childress[2,a] 〔iD〕

AFFILIATIONS

[1] Department of Physics, University of Basel, Klingelbergstrasse 82, 4056 Basel, Switzerland
[2] Department of Physics, McGill University, 3600 Rue University, Montreal, Quebec H3A 2T8, Canada
[3] Department of Physics, ETH Zürich, Otto-Stern-Weg 1, 8093 Zürich, Switzerland

[a] Author to whom correspondence should be addressed: lilian.childress@mcgill.ca

ABSTRACT

High-finesse, open-geometry microcavities have recently emerged as a versatile tool for enhancing interactions between photons and material systems with a range of applications in quantum optics and quantum information science. However, mechanical vibrations pose a considerable challenge to their operation within a closed-cycle cryostat, particularly when spatial tunability and free-space optical access are required. Here, we present the design and characterization of a system that can achieve ~16 pm-rms passive mechanical stability between two high-finesse mirrors with 34% duty cycle while permitting both three-dimensional positioning of the cavity mode and free-space confocal imaging. The design relies on two cascaded vibration isolation stages connected by leaf springs that decouple axial and lateral motion and incorporates tuned-mass and magnetic damping. Furthermore, we present a technique for quantifying cavity length displacements similar to or larger than the cavity linewidth, allowing for the *in situ* measurement of vibrations with and without active feedback. Our results facilitate operation of a tunable, high-finesse cavity within a closed-cycle cryostat, representing an enabling technology for cavity coupling to a variety of solid-state systems.

18 July 2024 13:27:08

I. INTRODUCTION

Fabry–Pérot microcavities offer an opportunity to engineer light–matter interactions with exquisite *in situ* control over the resonance frequency and location of the cavity optical mode. Such tunability enables the optimization of the cavity spectral and spatial overlap with a quantum emitter[1,2] and facilitates scanned imaging techniques.[3] Furthermore, open-geometry cavities can attain high quality factor to mode volume ratios by combining state-of-the-art mirror coatings with novel small-radius-of-curvature mirror substrates,[4,5] thereby strongly enhancing interactions between cavity-confined photons and quantum emitters. Moreover, by separating the optical resonator from the material system contained within, open microcavities can minimize fabrication-induced degradation of solid-state emitters.[6] As an example application, an open microcavity containing a nitrogen-vacancy (NV) center in a diamond membrane has been proposed as a mechanism to speed up entanglement distribution in quantum networks.[7]

For the most advanced applications, operation at cryogenic temperatures is essential to minimize the thermal phonon broadening present in solid-state systems. However, vibrations associated with cryostat operation make it challenging to achieve the mechanical stability required by high-finesse cavities while also maintaining the ability to position the cavity mode in three dimensions. Ideally, residual vibrations between the two cavity mirrors should be significantly less than the linewidth in length of the cavity optical resonance $\Delta L = \lambda/(2\mathscr{F})$, where λ is the resonant wavelength and $\mathscr{F}$ is the finesse; for example, $\Delta L \sim 30$ pm for $\lambda = 600$ nm and $\mathscr{F} = 10\,000$. For tunable systems based on wet cryostats, microcavity stability as low as 4.3 pm-rms[8] has been reported in a nitrogen-shield-free bath cryostat with the entire dewar acoustically shielded and resting on an actively vibrationally isolated platform. Closed-cycle cryostats offer an appealing alternative as they eliminate the need for expensive cryogenic liquids and allow the cavity to be operated over long time periods without cryogen refill interruptions. However, cryostat noise poses an even greater challenge in closed-cycle coolers, where the compressor and other moving parts

introduce a strong mechanical drive. In such systems, sub-pm-rms passive stability has only been achieved for a cavity without lateral tunability.[9] Among cryogenic cavity platforms with 3D cavity mode positioning, some also incorporate a proximal microscope objective to enable confocal sample imaging, optimal cavity mode out-coupling, and/or greater spatial precision in excitation: one showed a passive stability as low as ∼50 pm-rms[10] during quiet periods synchronized to the cryocooler cycle, while the other exhibited an overall stability of ∼120 pm-rms (passive) or ∼90 pm-rms (with active cavity locking).[11] A third system that has 3D cavity positioning, but appears not to incorporate a microscope objective, has shown ∼20 pm-rms quiet period stability with active cavity locking.[12]

Here, we present a cryogenic, widely tunable microcavity platform with microscopy-compatible optical access that achieves ∼16 pm-rms passive mechanical stability during cryocooler quiet periods. This performance is enabled by combining a rigid positioner with a home-built vibration isolation platform (VIP), which are both mounted within a commercially available table-top closed-cycle cryostat. In addition to isolating the cavity from noise along its axis, the VIP is designed to permit confocal imaging of the system via free-space optics with sub-micrometer resolution, requiring lateral rigidity and decoupling of axial (along the optical axis) motion. This free-space optical access also permits optimal cavity out-coupling and operation at wavelengths that induce fluorescence in fibers. We characterize the vibrations in our system using a technique that combines cavity transmission measurements with a Pound–Drever–Hall (PDH) error signal;[13] this approach makes it possible to characterize relatively large displacements *in situ* with a high-finesse cavity. We also consider active cavity locking at ambient and cryogenic temperatures and discuss implications for future improvements.

It is worth noting that the combination of inter-mirror stability and tunability required by microcavity applications is similar to the constraints on the tip–sample distance in advanced scanning probe microscopy (SPM) experiments. Indeed, closed-cycle cryogenic SPM systems with the stability at the picometer level have been achieved.[14–16] However, they are not compatible with free-space confocal imaging, as the SPM platform is typically suspended from highly compliant springs. The system and design principles presented here may thus also prove relevant to cryogenic SPM applications where precision optical imaging is needed.[17]

II. DESIGN OF THE APPARATUS

Our optical cavity comprises a macroscopic flat mirror and a small-radius-of-curvature mirror on the tip of an optical fiber (Thorlabs 630HP), as depicted in Fig. 1(a). The spherical dimple of the fiber mirror is machined using a laser ablation technique[18] with an interferometrically estimated radius of curvature $R = 65\ \mu m$. Both substrates are coated with dielectric Bragg mirrors (LASEROP-TIK) optimized to have high finesse at 637 nm (transmitted power: $T_{flat} = 190$ ppm and $T_{fiber} = 90$ ppm). The two mirrors are mounted on a three-axis positioner, which is, in turn, fixed to a home-built vibration isolation platform (VIP). The assembled system, mounted on the cryostat, can be seen in Fig. 1(b), with the flat mirror removed.

Ultimately, our goal is to reduce the effect of external vibrations on the relative motion between the cavity mirrors. The mechanical assembly binding the two mirrors effectively implements
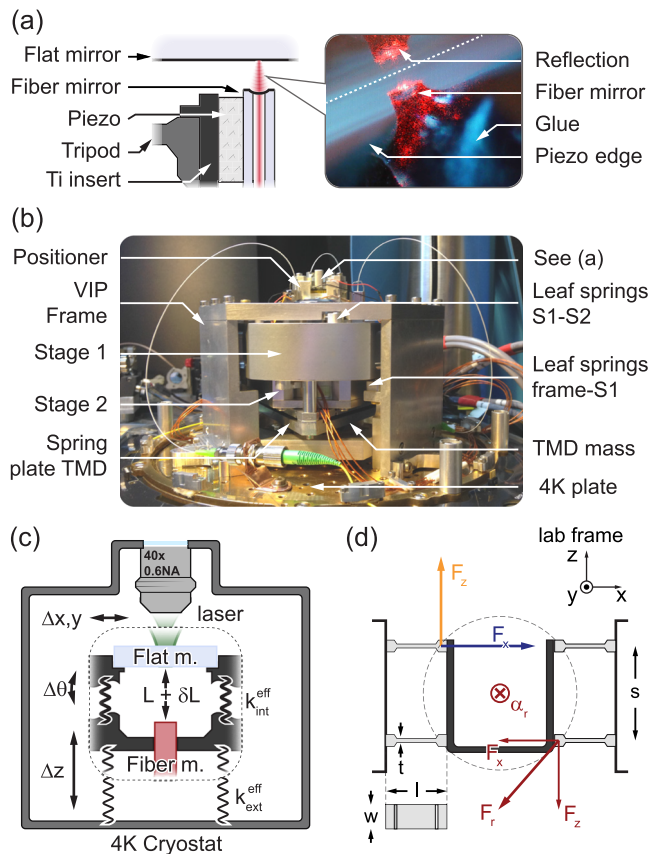
a mechanical high-pass filter, protecting the system against low-frequency components of the vibration spectrum. The cutoff frequency of this filter is determined by the mechanical resonance frequencies of the positioner, which are maximized by increasing the rigidity and reducing the effective mass. However, for stationary supporting elements of the positioner, a higher mass allows us to rapidly vary the mirror positions without significant backaction, which is crucial for active cavity stabilization. Thus, a trade-off should be sought regarding masses depending on the requirements of the system, while a high rigidity is always beneficial.

We employ a customized JPE (Janssen Precision Engineering) CPSHR3-S-COE sample positioner, which relies on a proprietary design to achieve long (∼mm) travel range in closed-loop mode while maintaining high rigidity with a specified unloaded axial (transverse) mechanical resonant frequency of 3.7 kHz (1.5 kHz).[19]

FIG. 1. Cavity and VIP design. (a) Schematic of the flat and fiber mirrors, shear piezo and titanium insert (left), and picture of the glued fiber (right). (b) Picture of the VIP and positioner supporting the cavity mounted on the 4 K plate of the cryostat. (c) Representation of the cryogenic scanning fiber cavity. The axial displacement (δL) is sensitive to external vibrations ($\ll$ nm). The additional external degrees of freedom of the positioner (where Δz is the axial translation, $\Delta x, y$ is the in-plane translation, and $\Delta \theta$ is the tilting motion) correspond to motion relative to the laboratory frame, thus impeding free-space optical access. (d) Concept of the dual-plane leaf-spring arrangement. Arrows depict a representative axial force (orange), transverse force (blue), and rotational forces and torque (red).

18 July 2024 13:27:08

Within the positioner, the mounting of the fiber and mirrors is also important to the mechanical properties of the system; the fiber is supported directly on the rigid housing of the positioner via a tripod, while the mirror can be moved. The fiber tip is facing upward and is glued to a high-frequency (~1 MHz unloaded) shear piezo, which allows for a fine adjustment of the fiber position along the optical axis (z), thereby tuning the cavity optical resonance [see Fig. 1(a)]. The piezo is mounted on a 3D-printed titanium insert, which is tightly nested in a tripod mount and held in position by a screw. To maximize the rigidity of the fiber mirror mount, we designed the tripod to have a high frequency (15 kHz) for its lowest-order drum-like mechanical mode and glued the fiber with minimal overhang to suppress cantilever oscillations. A close-up view of the assembled cavity is displayed in Fig. 1(a) (right), showing the fiber mirror and its reflection in the flat mirror.

In practice, the fundamental mechanical resonance frequency of a stepper positioner is limited to ~kHz by material properties and design considerations, setting an upper limit to the frequencies of noise it can reject. Nevertheless, by adding an isolation stage, it is possible to prevent problematic high-frequency noise from reaching the positioner.[20–22] In its simplest form, an isolation stage can be realized by suspending the apparatus with springs, effectively forming a harmonic oscillator acting as a low-pass filter. Softer springs or a heavier suspended mass lead to a lower cutoff frequency and therefore more aggressive filtering of the vibration spectrum. Various types of suspension systems (coil springs, levitation, and multiple stages) and damping strategies can be used depending on the particular application and the conditions in which the instrument operates (low temperature and vacuum).[21,23–26] For the most sensitive instruments, a combination of a rigid assembly and an isolation platform is necessary.

Our scanning cavity system is subject to a number of design constraints that are frequently encountered in modern setups: it operates in high vacuum (~1×10^{-6} mbar), at cryogenic temperature (a cryoplate temperature of 4 K), and in a table-top, closed-loop cryostat (a first-generation Montana Instruments Nanoscale Workstation). An additional set of constraints emerges from optical access requirements. We envision experimental applications that involve introduction of an optically active, solid-state sample (e.g., a diamond membrane containing single emitters) into the microcavity by bonding it to the flat mirror. Imaging the sample efficiently requires a high-numerical-aperture objective, which, in our apparatus, is fixed to the frame of the cryostat. Mounting the optic at room temperature allows us to use an off-the-shelf objective that is corrected for aberrations induced by our 2 mm-thick flat mirror. This implementation of external optical access precludes the use of an arbitrarily compliant isolation platform as it must be stiff enough to enable confocal imaging with sub-micrometer resolution. A generic depiction of such a setup is shown in Fig. 1(c). While the effective internal rigidity of the positioner k_{int}^{eff} should be as high as possible for all degrees of freedom, the constraints on the spring constant k_{ext}^{eff} of the vibration isolation platform can be summarized by three conditions:

1. k_{ext}^{eff} in the transverse (x, y) directions should be as high as possible ($\Delta x, y, \Delta \theta < 1~\mu$m),
2. k_{ext}^{eff} along the axial direction should be high enough to maintain our sample within the focal range ($\Delta z \sim 1~\mu$m), and

3. k_{ext}^{eff} along the axial direction should be minimized to prevent inter-mirror vibrations ($\delta L \sim 10$ pm-rms).

Conditions 1 and 3 require that the platform is engineered such that axial motion is effectively decoupled from other degrees of freedom. Conditions 2 and 3 indicate that a compromise must be made between vibration attenuation and relative motion between the objective and the sample in the axial direction. These conditions rule out the use of coil springs for suspension as their marginal transverse rigidity would lead to pendulum swing and rocking motion (corresponding to large $\Delta x, y$ and $\Delta \theta$ amplitudes). Furthermore, spring extension can lead to long, cumbersome assemblies, for which cooling the system without an exchange gas is impractical. One solution that fulfills all three conditions employs multiple stacked plates spaced by elastomeric joints, an approach commonly used in scanning probe apparatus.[21,27] In such designs, the reduced axial compliance is offset by the multiplication of the stages: the mechanical resonant frequency is higher, but the roll-off is steeper. However, operating at cryogenic temperature prevents the efficient use of elastomers as compliant, damping elements.

In order to circumvent these challenges, we propose a VIP based on leaf springs [design files available as supplementary material], which can be designed to attain a desired spring constant for bending while maintaining very high rigidity for all other deformation. A two-dimensional schematic of our "dual-plane" concept can be seen in Fig. 1(d), where a central platform (dark gray) is held by four leaf springs tethered to a rigid base. The springs are arranged on two horizontal planes separated by distance s. The motivation for this design can be understood by considering how the central platform displaces in response to axial (Δz, orange), transverse (Δxy, navy), and rotational ($\Delta \theta$, maroon) forces. The use of leaf springs allows us to separately engineer the response to transverse and axial forces. Using rectangular homogeneous beams with thickness t, width w, and length L as a toy model for the leaf springs, the ratios of resonant mechanical frequencies along the axial (thickness) direction z and the transverse directions x and y are simply

$$\frac{\omega_z}{\omega_x} = 2\sqrt{2}\frac{t}{L} \quad \text{and} \quad \frac{\omega_z}{\omega_y} = \frac{t}{w}, \tag{1}$$

allowing us to tune the axial compliance while maintaining transverse rigidity. In the case of a torque applied to the platform, a force acts on the springs with both F_z and $F_{x,y}$ components [red arrows in Fig. 1(d)]. The exact projections of the forces along z and x, y will depend on the geometry and distribution of the load on the platform; for the simple case of a platform with the center of rotation halfway between the two planes of springs, we find that the contribution of $F_{x,y}$ depends linearly on the inter-plane distance s. Consequently, for large s, the load transfer to axial bending is reduced, corresponding to an increase in torsional rigidity. By implementing such a dual-plane leaf-spring arrangement with a large inter-plane spacing s, axial motion can be effectively decoupled from all other modes.

We focused our design primarily on the axial modes since vibration isolation along the optical axis is the most stringent requirement. We tackled contradictory conditions 2 and 3 by nesting two platforms, hereby referred to as S1 and S2 [see Fig. 2(a)] where the positioner is mounted directly on S2. Such a cascaded setup allows us to maintain relatively high S1 (~50 Hz) and S2
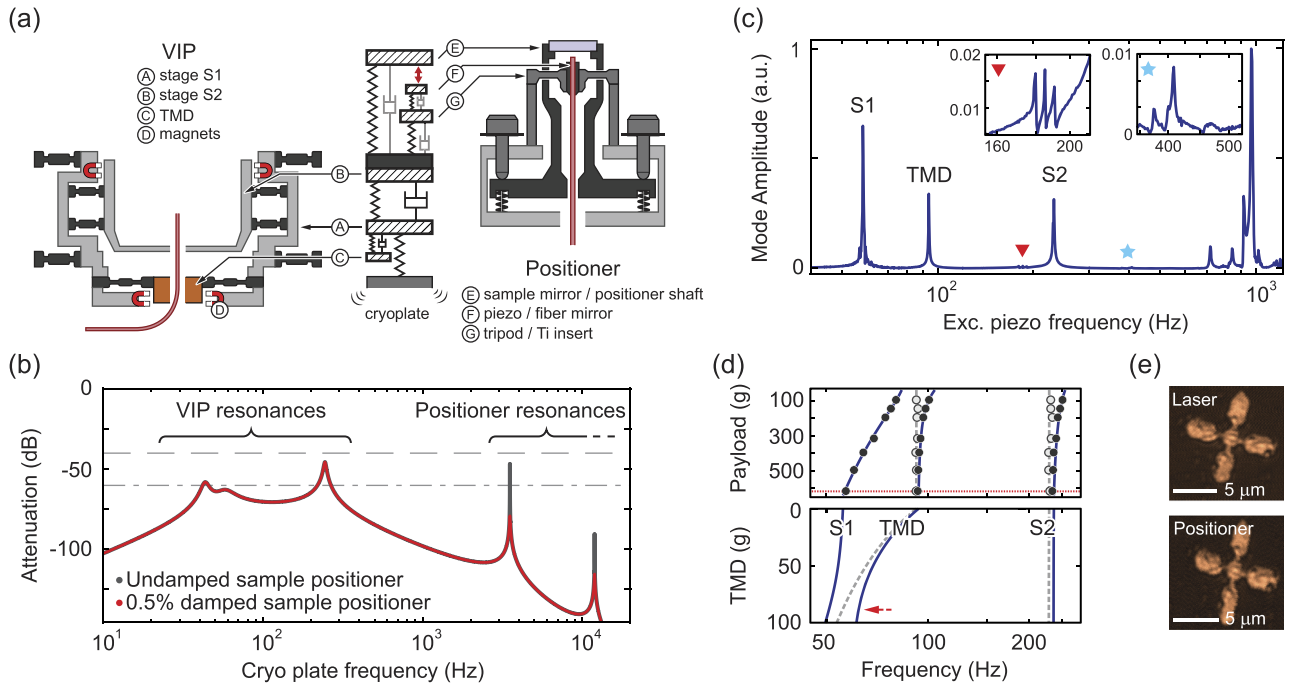
FIG. 2. VIP modeling and characterization: (a) one-dimensional damped mass-and-spring model for the passively stabilized cavity system, comprising the VIP (left) and the customized positioner (right), where the cryoplate drives the whole assembly. The fiber-sample spacing (cavity length) is indicated by a red arrow. (b) Calculated inter-mirror motional amplitude attenuation $20 \log(\delta L/A_{cryo})$ relative to the cryoplate motional amplitude (A_{cryo}) using the model in (a) with a TMD tuning-load of 87 g and a payload of 615 g. The dashed (dotted-dashed) line marks attenuation by a factor 10^2 (10^3). (c) Sample mirror axial motion measured with respect to the lab frame upon excitation by a piezo located on S1, without any tuning-load and with a payload of 615 g (mass of the positioner). The main VIP axial modes (corresponding to S1, S2, and the out-of-tune TMD) are labeled. Insets depict residual motion attributed to rocking of S1 and S2. The high-frequency peaks near 1 kHz are assigned to localized, higher-order modes, or the positioner internal mechanical resonances. (d) Frequencies of the three main VIP mechanical resonances (gray solid circles) and two anti-resonances (black empty circles) measured while changing the VIP payload without tuning-load (top). The red dotted line indicates the payload corresponding to the positioner. Blue solid and gray dashed lines are fits to a model comprising three masses and springs. The fit parameters are used to extrapolate the necessary tuning-load of 90 g (bottom, an optimal value indicated by a red dashed arrow). (e) Reflection confocal microscopy images of markers on the sample taken by scanning the laser beam (top) or the positioner piezos (bottom) during cryostat operation.

(~230 Hz) resonant mechanical frequencies while benefiting from increased roll-off at higher frequencies.[21] Given the target resonant frequencies of S1 and S2 and the approximate load, we designed the springs to have the necessary rigidity by using basic beam theory estimates followed by a more complete calculation using a finite element analysis software.[28] We then fine-tuned the geometrical parameters to obtain resonant axial modes at the target frequencies while maximizing the frequency of all other modes (rocking, twisting, and lateral translation).

Another essential element of the isolation design is damping, as it suppresses large-amplitude motion at the platform resonant frequencies. Unfortunately, operating at cryogenic temperature precludes the use of elastomers as damping elements, while dashpot-type damping is incompatible with vacuum. Since adding significant damping directly to the S1 platform would decrease the roll-off past mechanical resonance, we employ eddy-current magnet braking[29] applied on a tuned-mass damper (TMD) anchored to S1 with a spring plate.[30] The spring plate in itself contributes to the effective mass of the TMD mechanical mode. This mass is further increased by attaching a tuning-load made of copper to the spring plate. The tuning-load mass is chosen so that the first axial mode of the TMD

hybridizes with the S1 mode; upon excitation, the energy is transferred back and forth between the platform and the TMD, which, in turn, is damped by a set of six samarium cobalt (SmCo) magnets arranged around the tuning-load to minimize the stray magnetic field at the sample location. Due to spatial constraints, S2 is damped directly by three pairs of SmCo magnets arranged with the same consideration, resulting in a reduction in roll-off that comes as an engineering compromise. We further obtain damping by constructing all other components from aluminum, which has a comparatively high residual damping parameter among different metals at low temperature. This material choice carries other considerations as well. Aluminum has a ratio of Young's modulus to weight roughly equivalent to stainless steel and titanium, yet it is easily sourced and machined with modern tools, ensuring a finished product with tight tolerances. Furthermore, while aluminum has the disadvantage of high thermal contraction, in principle, it provides excellent thermal conductivity; our observed sample temperature of ~11 K (a cryoplate nominal temperature of 4 K) was likely limited by imperfect thermal contacts, which could be improved by application of indium or other thermally conductive material.

As discussed above, our leaf-spring-based, dual-plane arrangement essentially decouples the axial modes from other mechanical modes, allowing us to model our stage and positioner as a 1D system of coupled harmonic oscillators. Figure 2(a) shows representative schematics of the VIP (left) and the JPE positioner (right) as well as the equivalent model, which can be used to calculate the amplitude of cavity length excursions δL (red arrow) as a function of the amplitude of cryoplate displacement A_{cryo} (the main source of mechanical noise) over a range of frequencies. The results, expressed as $20 \log(\delta L/A_{\text{cryo}})$, can be seen in Fig. 2(b) for two different values of positioner damping, where the dashed (dotted-dashed) line indicates an attenuation of $\delta L/A_{\text{cryo}} = 10^{-2}$ (10^{-3}). The mechanical resonances of the VIP (positioner) are clearly visible at low (high) frequencies. Larger frequency splitting between VIP and positioner modes leads to larger attenuation over the full spectrum; at frequencies below the positioner resonances, the two mirrors move together, while at frequencies above the VIP resonances, the amplitude of transmitted oscillations is strongly suppressed.

To characterize the VIP, we measured the resonance frequency of its mechanical modes using an unbalanced Michelson interferometer under ambient conditions. One arm of the interferometer served as a reference, while the mirror of the second arm was mounted on the VIP top platform (S2). Measurements were performed using a tunable 637 nm laser with its wavelength adjusted to maximize the sensitivity of the resulting photodiode signal. The laser frequency was then locked to the diode signal, resulting in a frequency detuning that was directly proportional to the axial motion of S2. A piezo shaker, mounted off-center on the bottom platform S1, provided a local source of excitation. The shaker was driven by a lock-in amplifier, which was also used to demodulate the measured motion of S2 and the sample mirror, allowing us to strongly drive the stage and measure its response with an excellent signal-to-noise ratio.

The VIP spectral response comprises three main peaks in the 50–320 Hz range [see Fig. 2(c)] that correspond to modes stemming from the TMD, S1, and S2. The insets of Fig. 2(c) provide a close-up of low-amplitude modes around 200 and 400 Hz related to rocking motion of S1 and S2. These resonance triplets mirror the three-fold symmetry of the stage, slightly broken by the off-center drive and load imbalance. At higher frequencies, large-amplitude peaks start to appear that cannot be attributed with certainty but probably originate either from local internal vibrational modes of S1 excited by the piezo shaker or the positioner internal transverse mechanical resonances. Provided that these modes are localized, their role in transferring vibrations from the cryoplate should be minimal. The spectrum in Fig. 2(c) was acquired with a full payload (the positioner) but without any TMD tuning-load; in order to find the correct tuning-load mass leading to S1 and TMD mode hybridization, we varied the payload from 100 to 615 g and recorded the position of the three main mechanical resonances and two anti-resonances [Fig. 2(d), top]. We then fit a three-harmonic-oscillator model to retrieve the effective masses and spring constants and infer a best value for the tuning-load of ~90 g for the full payload [Fig. 2(d), bottom].

The low amplitudes and relatively high frequencies of the rocking modes detected in Fig. 2(c) indicate a high rocking and in-plane mode rigidity, necessary to fulfill condition 1 for imaging. With the full system mounted on the cryostat, we verified that we can image a micrometer-sized alignment marker by scanning either the

laser beam or the fine piezos of the JPE [Fig. 2(e)] during cryostat operation. Both images clearly resolve sub-micrometer features. The distortion in the piezo scan is due to the piezo hysteresis and the particular actuation mode of the positioner. Importantly, the resolution is maintained despite driving the positioner piezo in steps and at a high rate (several hundred Hz).

III. CAVITY LENGTH CALIBRATION

We quantify the performance of the vibration isolation system by characterizing the transmission and reflection properties of the cavity it supports using laser light near 652 nm. Notably, to increase the dynamic range for measuring cavity length excursions when working with high-finesse cavities, we have developed a technique that combines measurements of cavity transmission and a Pound–Drever–Hall (PDH) error signal.[13] The transmission is symmetric about the cavity optical resonance, whereas the PDH signal is antisymmetric [see Fig. 3(a)] such that the combined measurement allows us to unambiguously determine the cavity length excursion even for fluctuations comparable to the full cavity linewidth. This approach is applicable both with the cavity free-running and when we use the PDH error signal to lock the cavity to the reference laser.

The first step in measuring cavity length excursions is to calibrate the cavity transmission and PDH error signal as a function of
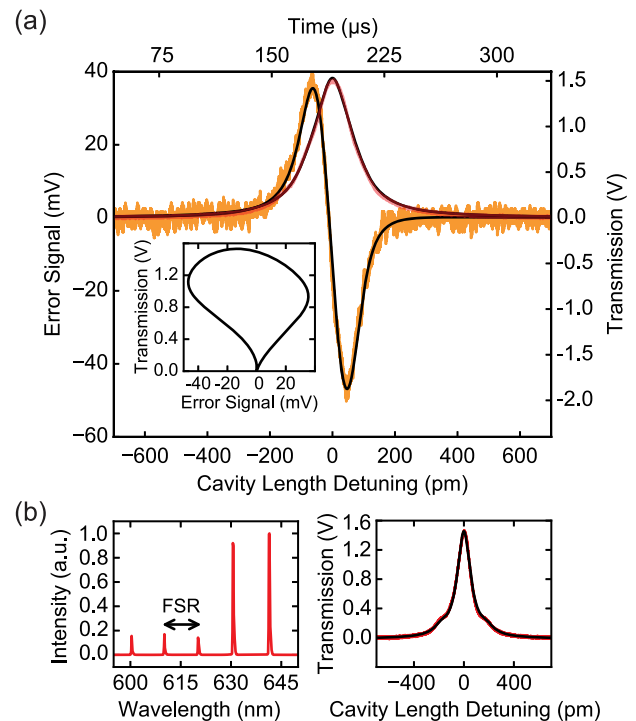

FIG. 3. Cavity parameter extraction. (a) Simultaneously acquired transmission (red) and error signal (orange) as a function of cavity length with joint analytic fit overlaid (black). The inset shows the parametric plot of the fit. (b) Cavity broadband transmission spectrum (left), used to extract the cavity length from the FSR ($L = 18.7 \pm 0.7\ \mu$m), and transmission of a 652.6 nm laser with sidebands at 4.5 GHz (right), used to determine the cavity linewidth ($\Delta\nu = 3.0 \pm 0.3$ GHz).

the cavity length. Essentially, we convert measured signals as a function of time (as we displace a cavity mirror) to signals as a function of length by fitting our data to functional forms incorporating the cavity linewidth in length ΔL (see Fig. 3). The appropriate analytical expressions are found by calculating transmission and PDH error signals for a cavity with a complex coupling coefficient[31] and are given in the supplementary material. We determine the linewidth in length ΔL via the finesse $\mathscr{F}$ = FSR/$\Delta \nu$, which is the ratio of two quantities that we can directly measure: the cavity free spectral range [FSR, measured by white light transmission; see Fig. 3(b), left] and the cavity linewidth in frequency [$\Delta \nu$, obtained from the cavity transmission of a phase-modulated laser whose sideband spacing provides a frequency reference; see Fig. 3(b), right]. Matching the fitted linewidth in time to the known linewidth in length calibrates the x axis for the error signal and transmission.

We can readily confirm that combined measurements of the transmission and PDH error signal provide a unique determination of cavity length displacement by verifying that they do not self-intersect when plotted parametrically [see the inset of Fig. 3(a)]. In practice, our measurement noise leads to overlapping data near the origin for positive and negative excursions that are significantly larger than the cavity linewidth ΔL. Therefore, to maximize the dynamic range of our displacement measurement, we work with a lowered cavity finesse $\mathscr{F}$ = 2700 ± 20 by using a long cavity (L = 18.7 ± 0.7 μm) where clipping losses dominate,[32] resulting in a linewidth of ΔL = 124 ± 1 pm.

To acquire data on our cavity length fluctuations, we take noisy time traces of the error signal $E_i \pm \sigma_E$ and transmission $T_i \pm \sigma_T$, as shown in Figs. 4(a) and 4(b). Here, the solid line shows the fits from Fig. 3(a), scaled and offset to best fit the dataset [accounting for drifts in laser power and residual amplitude modulation (RAM) in the error signal]. Each point $[E(\delta L), T(\delta L)]$ on the solid line thus corresponds to a known cavity length detuning δL. Measurement noise creates some spread in the data around the ideal values. Thus, for a given measurement ($E_i \pm \sigma_E$, $T_i \pm \sigma_T$), we infer the length detuning δL_i by minimizing the noise-weighted distance [$r(\delta L_i)$] between points (E_i, T_i) and $[E(\delta L_i), T(\delta L_i)]$, given by

$$r(\delta L_i) = \sqrt{\left(\frac{E_i - E(\delta L_i)}{\sigma_E}\right)^2 + \left(\frac{T_i - T(\delta L_i)}{\sigma_T}\right)^2}. \quad (2)$$

For far-detuned cavities, both signals approach zero, so a sequence of measurements may be erroneously inferred to jump from far-positive to far-negative detuning. This is mitigated by limiting the range of δL_i during the minimization procedure to $\delta L_{i-1} \pm 100$ pm; the inset of Fig. 4(c) illustrates the effect of this restriction. Notably, this limitation on δL_i decreases our estimate of the full-cycle rms motion by just 0.5 pm, consistent with the elimination of spurious jumps from far-positive to far-negative detuning.

IV. RESULTS

The data in Fig. 4 are acquired with the cavity free-running near optical resonance (unlocked), allowing us to evaluate the performance of our passive vibration isolation system. Even in the raw data, one can see that the cavity vibrations are strongly influenced by the cold-head cycle of our cryostat. We therefore divide the dataset into noisy (orange) and quiet (red) periods, which, in
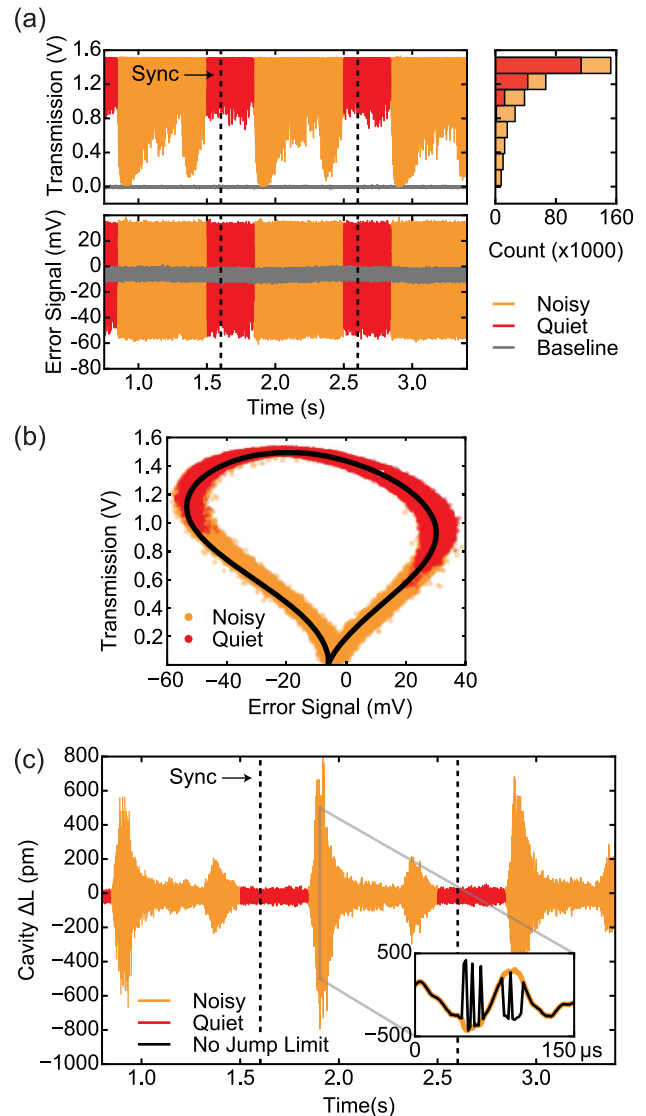

FIG. 4. Unlocked cavity measurements. (a) Segments of the transmission and the error signals as a function of time. The sync signal from the cryostat is indicated with a dotted vertical line and is used to distinguish between quiet periods (red) and noisy periods (orange). Baseline (off-resonance) noise is also shown (gray). Histogram of transmission data demonstrates that the cavity remains near resonance for the majority of the trace. (b) Parametric plot of transmission and error signal from the data in (a), with quiet (red) and noisy (orange) data, and the analytic fit overlaid. (c) Cavity length excursion obtained from data in (a) assuming a 100 pm maximum jump in length between data points. Inset: a comparison with (orange) and without (black) the maximum jump restriction, taken during a noisy period (the region indicated by a vertical, gray solid line).

post-processing, are timed relative to a sync pulse provided by the cryostat. We note that the quiet period data are more reliable: as shown in Fig. 4(b), data acquired during the quiet period never approach the origin of the parametric curve, staying far from the region where the curve intersects itself and thus producing unambiguous measurements of cavity displacement. Consequently, within

the quiet period, we extract a reliable measurement of 16 ± 1 pm-rms, while the estimate of motion over the full cold-head cycle (54 ± 4 pm-rms) likely suffers from systematic errors. Here, the error bars are statistical errors extracted from the standard deviation of multiple measurements. The excellent passive stability achieved during the quiet region, which comprises ~34% of the complete cold-head cycle, creates an opportunity to perform measurements without the overhead of active cavity stabilization.

We can use the same measurement technique to characterize cavity vibrations while the cavity is actively stabilized. We lock the cavity to the laser frequency by feeding the PDH error signal back to the shear piezo on which the fiber mirror is mounted [Fig. 1(d)]. Figure 5(a) shows the rms vibrations of the cavity with and
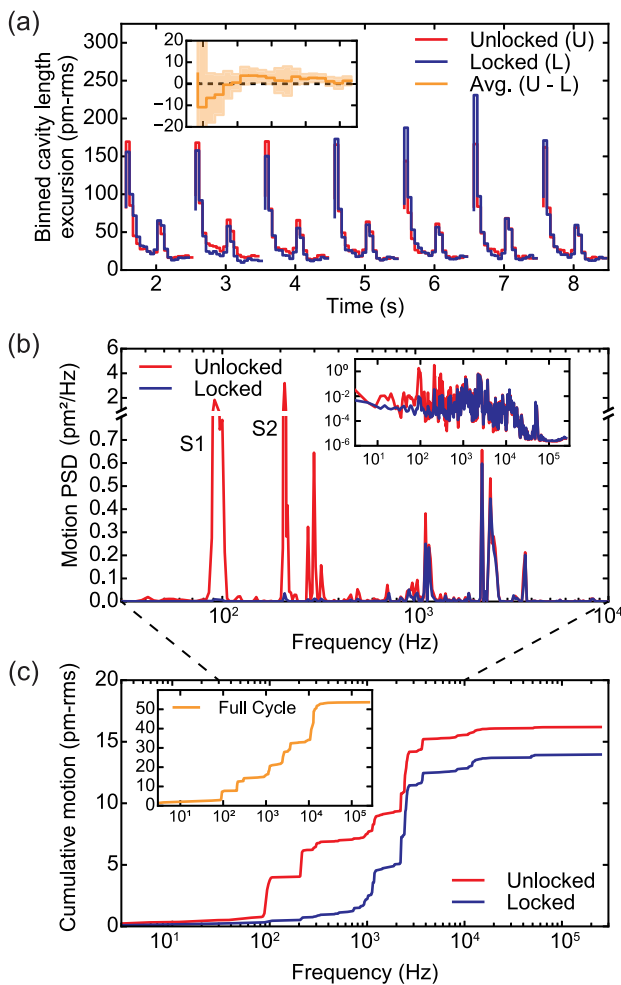

FIG. 5. Locked cavity measurements. (a) The rms value of the cavity length excursions in 50 ms time bins for the locked (blue) and unlocked (red) cavity. Inset: Averaged difference in rms motion between unlocked and locked cycles. The error bars denote the statistical uncertainty from averaging nine cycles. (b) PSD of length noise on a linear scale, with assignments of low-frequency peaks to VIP stage mechanical resonances (inset: log scale). (c) Cumulative cavity length excursion (rms) of the quiet period for the locked (blue) and unlocked (red) cavity. Inset: Full-cycle, unlocked (orange) cumulative cavity length excursion (rms).
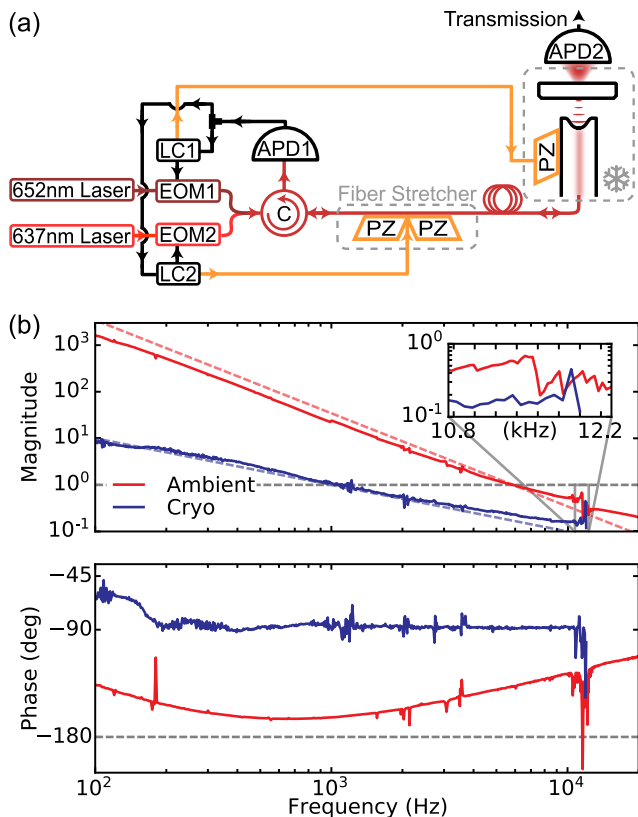
without active stabilization, calculated in 50 ms intervals throughout the cold-head cycle, indicating that cavity locking does not substantially improve the performance of our system.

Frequency-domain analysis provides a greater insight into the performance of both passive and active stabilization. The power spectrum of vibrations during the quiet period is shown in Fig. 5(b) for a free-running (red) and locked (blue) cavity. Active stabilization clearly improves rejection of low-frequency noise, up to ~1 kHz, but fails to suppress the dominant high-frequency noise. In fact, we see an increase in 1–3 kHz noise when active stabilization is enabled, as illustrated by the quiet period cumulative distribution in Fig. 5(c). Integrating the noise up to 250 kHz, we find an rms motion of 14.0 ± 0.9 pm-rms for the actively stabilized cavity during the quiet periods, which is a marginal improvement over the 16 ± 1 pm-rms measured for the free-running cavity.

This frequency-domain analysis also reveals the mechanical resonances associated with the vibration isolation platform and the positioner. In particular, low-frequency peaks S1 and S2 are shifted from their design values due to a combination of change in Young's modulus with temperature and thermal contraction such that the TMD becomes out-of-tune at low temperature. The absence of a visible TMD peak offers additional evidence that the TMD is not performing as designed. Improved modeling that takes into account the shifts in material properties with temperature may offer a route to further improve the passive vibration isolation performance.

The surprisingly poor performance of the active stabilization is rooted in several elements of our apparatus. One limitation arises from the finite dynamic range of our error signal, which approaches zero for displacements exceeding approximately the cavity linewidth. In the presence of large-amplitude disturbances, the feedback gain becomes nonlinear and, for extreme displacements, insufficient to maintain the lock. The dynamic range can be increased while maintaining the lock sensitivity by either decreasing cavity finesse (at the cost of higher laser power) or increasing the modulation frequency used for PDH locking (with diminishing effect once in the resolved-sideband limit).

This finite dynamic range poses an even greater problem in the presence of fluctuations in the error-signal offset, which create a second zero-crossing point in the error signal. This marks the onset of positive feedback, pushing the cavity resonant frequency away from that of the laser. In our system, such an offset arises from residual amplitude modulation (RAM) in the incident light, caused by a low-finesse interferometer formed between our fiber mirror and a weak reflection off the circulator, which converts phase modulation (introduced for PDH locking) into amplitude modulation with an efficiency that varies with interferometer length. Even after optimizing our phase modulation frequency,[33] small changes in the length of the optical fiber between our circulator and fiber mirror (due to variations in temperature and strain) induced significant fluctuations in the error-signal offset. To maintain a robust cavity lock, it was therefore necessary to add a second, independent PDH feedback loop to actively stabilize the cavity fiber length [see Fig. 6(a)] using a homemade fiber stretcher. While this solution allowed us to maintain a cavity lock on the order of minutes, the slow variation in peak rms motion observed during the noisy periods in Fig. 5(a) is likely an artifact of remaining weak RAM fluctuations.

The final and most critical challenge to active stabilization is the high frequency ~kHz noise present in our system. We can

FIG. 6. Cavity-locking setup and characterization. (a) Experimental schematic: two lasers (652 and 637 nm) are phase modulated via electro-optic modulators (EOM1, 2) at 1.16 GHz and 305 MHz, respectively; the beams are combined at the input of a circulator (C) with powers of 1.7 mW and 125 μW and subsequently directed toward the fiber mirror. The reflected light is routed via the circulator to an avalanche photodiode (APD1), and the detector output is demodulated by two analog PDH circuits (LC1, 2). The resulting error signals (shown in yellow) are fed back to two piezo-electric transducer (PZ) circuits: the first (which uses the 652 nm laser) adjusts the position of the cavity mirror and, therefore, the cavity length, and the second (using the 637 nm laser) controls a stretcher for the cavity fiber. The light transmitted through the cavity is free-space coupled to a second detector (APD2). (b) Ambient (red) and low temperature (blue) cavity locking circuit transfer functions. Blue (red) dashed lines indicate one (two) poles of roll-off. The gray dashed line indicates the ringing condition of a magnitude of 1 and a phase of −180°, around which the phase response is unwrapped. Inset: amplitude of the resonance that limits the locking bandwidth.

characterize the frequency-dependent performance of our lock by its transfer function $G(f)$,[34] where cavity vibrations are suppressed by $|1 + G(f)|$ when locked; Fig. 6(b) shows the magnitude and phase of $G(f)$ for both ambient (red) operation and cryogenic (blue) operation. Prior to cooling down, we optimized our feedback system under ambient conditions and found that it was possible to achieve a ~10 kHz lock bandwidth [defined as the lowest frequency where $|G(f)| = 1$] and nearly two poles of roll-off at low frequencies, leading to a factor of 40–50 suppression in noise at 1 kHz and ~2 orders of magnitude reduction in rms motion overall.

Unfortunately, the performance at cryogenic temperatures was markedly worse. While the ringing frequency (~11 kHz) did not

change significantly upon cooldown, we were not able to achieve a stable lock with two poles of roll-off at low frequencies or a bandwidth beyond 1 kHz without inducing ringing. These difficulties likely result from the change in material properties (most notably a reduction in material damping) at low temperature. Indeed, the resonance near 11 kHz shows a large increase in amplitude (and decrease in width), which prevented us from further increasing the gain or introducing filters that decrease the phase near this frequency. This resonance is likely of mechanical origin and associated with the tripod support for the fiber mirror, which could be improved through careful mechanical engineering. The relative insensitivity of the frequency upon cooldown, while surprising, could arise from the complicated interplay of thermal contraction, slippage, and change in Young's modulus. Such elusive details would justify a more complete characterization and modeling of the mechanical resonances of the system at cryogenic temperatures, which would allow for an improved filter design, bringing the cryogenic transfer function closer to the optimized ambient system and potentially enabling 1–2 orders of magnitude improvement in system stability.

V. CONCLUSION AND OUTLOOK

The design reported and characterized here enables a widely tunable yet stable mechanical system within a table-top closed-cycle cryostat. Combining our home-built vibration isolation platform with a customized commercial positioner realizes a system with mm-scale tunability and 10 μm-scale fine control that, nevertheless, demonstrates excellent passive stability (16 pm-rms) during quiet periods of the cold-head cycle. Notably, our design exhibits this stability in an early-generation table-top closed-cycle cryostat that has its Gifford–McMahon cryocooler mounted on the optical table next to the sample chamber. Using a newer or heavily modified cryostat design that better decouples the closed-cycle cooler from the cold plate would lead to immediate improvements.[15,16,25] Moreover, the system would benefit from further optimization of the mechanical design, specifically that of the TMD at cryogenic temperature, and the structures of the tripod and fiber insert. The tripod plays a crucial role for active feedback, and increasing both its mass and mechanical resonance frequency would lead a to higher locking bandwidth by shifting the limiting mechanical resonance and diminishing its amplitude. Similarly, a more integrated insert mechanism would ensure that the insert itself does not introduce unwanted localized mechanical modes within the locking bandwidth of the system.

While there is substantial room to improve active cavity locking, there are also advantages to working with a passively stable apparatus. The lock wavelength used here was chosen for convenience but, in an experiment, would need to be carefully selected to eliminate undesired interactions between the system of interest and the lock laser. Fortuitously, the passive stability demonstrated here already enables significant applications for cryogenic microcavities without the need for locking.

In particular, we can quantify the applicability of our passively stabilized system to cavity quantum electrodynamic experiments with solid-state emitters. When spatially and spectrally tuned to the emitter, a cavity enhances the rate of resonant emission by the so-called Purcell factor. Vibrations reduce this effect as the cavity optical mode is no longer on resonance with the emitter transition at all

times. Assuming Gaussian statistics for cavity length excursions, the Purcell factor in the presence of vibrations is given by $F_p + 1$, with

$$F_p(\sigma) = F_p^0 \sqrt{\frac{\pi}{8}} \frac{\Delta L}{\sigma} e^{\Delta L^2 / 8\sigma^2} \left(1 - erf\left(\frac{\Delta L}{2\sqrt{2}\sigma}\right)\right), \qquad (3)$$

where $F_p^0 + 1$ is the resonant Purcell factor, ΔL is the cavity linewidth in length, and σ is the rms cavity-length excursion. For example, for a cavity with a finesse $\lambda/(2\Delta L) = 16\,000$ at $\lambda = 637$ nm and $\sigma = 16$ pm-rms, as observed during quiet periods of our system, only a moderate reduction in Purcell enhancement occurs, $F_p/F_p^0 = 0.5$.

This level of stability is particularly promising for the long-standing challenge of achieving a cooperativity >1 interface between optical cavities and NV centers in diamond. Using realistic parameters from recent papers, we consider a cavity with a finesse of 11 000 in a diamond-like mode[35] and a fiber mirror radius of curvature of 16 μm.[36] We assume an NV center with ideal orientation, location and quantum efficiency, a membrane of thickness 3.8 μm,[6] and an air gap of ~2 μm.[37] With these assumptions and the 16 pm-rms vibrations we observe here, we predict a Purcell enhancement of more than 250, which, combined with a ZPL fraction of 3% and a linewidth of 86 MHz, corresponds to a cooperativity just over 1. In particular, the residual vibrations of this hypothetical system reduce its performance by less than 40%. Thus, even without active stabilization, it should be possible to observe a large Purcell enhancement of narrow-linewidth emitters, speeding up probabilistic entanglement distribution methods.[38] Cavity enhancement of the zero-phonon-line collection efficiency offers a significant advantage even at the cost of 1/3 duty cycle, and the ~0.34 s quiet periods are long enough for experiments exploiting the exceptional coherence times of NV spins. Looking forward to future improvements, stable microcavity systems could even push toward the high-cooperativity regime and "always-on" operation, potentially offering a platform for near-deterministic quantum network protocols.

AUTHORS' CONTRIBUTIONS

Y.F. and R.Z. contributed equally to this work.

SUPPLEMENTARY MATERIAL

The supplementary material offers additional technical documentation of our vibration isolation design and analysis technique. We provide computer-aided design (CAD) files in the STEP format for the vibration isolation platform; note that similar CAD files for the positioner can be downloaded directly from the manufacturer.[19] We also provide a Mathematica notebook containing a derivation of the transmission and error signal as a function of cavity length, which we employ in our measurements of cavity length excursions.

ACKNOWLEDGMENTS

DATA AVAILABILITY

The data that support the findings of this study are available from the corresponding author upon reasonable request.

REFERENCES

[1]F. Li, Y. Li, Y. Cai, P. Li, H. Tang, and Y. Zhang, Adv. Quantum Technol. **2**, 1900060 (2019).

[2]D. Najer, I. Söllner, P. Sekatski, V. Dolique, M. C. Löbl, D. Riedel, R. Schott, S. Starosielec, S. R. Valentin, A. D. Wieck, N. Sangouard, A. Ludwig, and R. J. Warburton, Nature **575**, 622 (2019).

[3]M. Mader, J. Reichel, T. W. Hänsch, and D. Hunger, Nat. Commun. **6**, 7249 (2015).

[4]A. A. P. Trichet, P. R. Dolan, D. M. Coles, G. M. Hughes, and J. M. Smith, Opt. Express **23**, 017205 (2015).

[5]D. Najer, M. Renggli, D. Riedel, S. Starosielec, and R. J. Warburton, Appl. Phys. Lett. **110**, 011101 (2017).

[6]M. Ruf, M. IJspeert, S. van Dam, N. de Jong, H. van den Berg, G. Evers, and R. Hanson, Nano Lett. **19**, 3987 (2019).

[7]F. Rozpędek, R. Yehia, K. Goodenough, M. Ruf, P. C. Humphreys, R. Hanson, S. Wehner, and D. Elkouss, Phys. Rev. A **99**, 052330 (2019).

[8]L. Greuter, S. Starosielec, D. Najer, A. Ludwig, L. Duempelmann, D. Rohner, and R. J. Warburton, Appl. Phys. Lett. **105**, 121105 (2014).

[9]B. Merkel, A. Ulanowski, and A. Reiserer, Phys. Rev. X **10**, 041025 (2020).

[10]M. Ruf, M. Weaver, S. van Dam, and R. Hanson, Phys. Rev. Appl. **15**, 024049 (2021).

[11]S. Vadia, J. Scherzer, H. Thierschmann, C. Schäfermeier, C. D. Savio, T. Taniguchi, K. Watanabe, D. Hunger, K. Karraï, and A. Högele, arXiv:2103.05619 (2021).

[12]B. Casabone, C. Deshmukh, S. Liu, D. Serrano, A. Ferrier, T. Hümmer, P. Goldner, D. Hunger, and H. de Riedmatten, arXiv:2001.08532 (2020).

[13]E. D. Black, Am. J. Phys. **69**, 79 (2001).

[14]J. D. Hackley, D. A. Kislitsyn, D. K. Beaman, S. Ulrich, and G. V. Nazin, Rev. Sci. Instrum. **85**, 103704 (2014).

[15]S. Zhang, D. Huang, and S. Wu, Rev. Sci. Instrum. **87**, 063701 (2016).

[16]S. Chaudhary, J. J. Panda, S. Mundlia, S. Mathimalar, A. Ahmedof, and K. V. Raman, Rev. Sci. Instrum. **92**, 023906 (2021).

[17]M. Pelliccione, A. Jenkins, P. Ovartchaiyapong, C. Reetz, E. Emmanouilidou, N. Ni, and A. C. B. Jayich, Nat. Nanotechnol. **11**, 700 (2016).

[18]D. Hunger, T. Steinmetz, Y. Colombe, C. Deutsch, T. W. Hänsch, and J. Reichel, New J. Phys. **12**, 065038 (2010).

[19]JPE B.V., https://www.jpe-innovations.com/, 2021.

[20]D. W. Pohl, IBM J. Res. Dev. **30**, 417 (1986).

[21]M. Okano, K. Kajimura, S. Wakiyama, F. Sakai, W. Mizutani, and M. Ono, J. Vac. Sci. Technol. A **5**, 3313 (1987).

[22]S. I. Park and C. F. Quate, Rev. Sci. Instrum. **58**, 2004 (1987).

[23]G. Binnig, H. Rohrer, C. Gerber, and E. Weibel, Appl. Phys. Lett. **40**, 178 (1982).

[24]C. R. Ast, M. Assig, A. Ast, and K. Kern, Rev. Sci. Instrum. **79**, 093704 (2008).

[25]W. Zhang, J. M. Robinson, L. Sonderhouse, E. Oelker, C. Benko, J. L. Hall, T. Legero, D. G. Matei, F. Riehle, U. Sterr, and J. Ye, Phys. Rev. Lett. **119**, 243601 (2017).

[26] M. de Wit, G. Welker, K. Heeck, F. M. Buters, H. J. Eerkens, G. Koning, H. van der Meer, D. Bouwmeester, and T. H. Oosterkamp, Rev. Sci. Instrum. **90**, 015112 (2019).

[27] A. I. Oliva, M. Aguilar, and V. Sosa, Meas. Sci. Technol. **9**, 383 (1998).

[28] Ansys® Workbench, 17th ed., Ansys, Inc., 2016.

[29] H. A. Sodano, J.-S. Bae, D. J. Inman, and W. K. Belvin, J. Vib. Acoust. **128**, 294 (2006).

[30] H. Frahm, U.S. Patent No. 989, 958 (April 18, 1911).

[31] E. Janitz, M. Ruf, M. Dimock, A. Bourassa, J. Sankey, and L. Childress, Phys. Rev. A **92**, 043844 (2015).

[32] J. Benedikter, T. Hümmer, M. Mader, B. Schlederer, J. Reichel, T. W. Hänsch, and D. Hunger, New J. Phys. **17**, 053051 (2015).

[33] P. Ehlers, A. C. Johansson, I. Silander, A. Foltynowicz, and O. Axner, J. Opt. Soc. Am. B **31**, 2938 (2014).

[34] J. Bechhoefer, Rev. Mod. Phys. **77**, 783 (2005).

[35] R. H. Jensen, E. Janitz, Y. Fontana, Y. He, O. Gobron, I. P. Radko, M. Bhaskar, R. Evans, C. D. R. Rosenblueth, L. Childress, A. Huck, and U. L. Andersen, Phys. Rev. Appl. **13**, 064016 (2020).

[36] D. Riedel, Ph.D. thesis, University of Basel, 2017.

[37] D. Riedel, I. Sollner, B. J. Shields, S. Starosielec, P. Appel, E. Neu, P. Maletinsky, and R. J. Warburton, Phys. Rev. X **7**, 031040 (2017).

[38] P. C. Humphreys, N. Kalb, J. P. J. Morits, R. N. Schouten, R. F. L. Vermeulen, D. J. Twitchen, M. Markham, and R. Hanson, Nature **558**, 268 (2018).

18 July 2024 13:27:08